CORA Cork Open Research Archive
Cartlann Taighde Oscailte Chorcaí

Title	Tunable power-phase distributions in a phonon-magnon-coupled magnon microwave antenna for reservoir computing
Authors	Samanta, Arindam;Roy, Saibal
Publication date	2024-11-26
Original Citation	Samanta, A. and Roy, S. (2024) 'Tunable power-phase distributions in a phonon-magnon-coupled magnon microwave antenna for reservoir computing', Physical Review Applied, 22(5), 054076 (18pp). https://doi.org/10.1103/PhysRevApplied.22.054076
Type of publication	Article (peer-reviewed)
Link to publisher's version	10.1103/PhysRevApplied.22.054076
Rights	© 2024, American Physical Society. All rights reserved.
Download date	2026-11-16 10:05:53
Item downloaded from	https://hdl.handle.net/10468/16712



UCC
University College Cork, Ireland
Coláiste na hOllscoile Corcaigh

Tunable power-phase distributions in phonon-magnon-coupled magnon microwave antenna for reservoir computing

Arindam Samanta [1,2,*] and Saibal Roy [1,2,†]

[1] *Micropower Devices and Nanomagnetics Group, Tyndall National Institute, Cork, T12 R5CP, Ireland*
[2] *School of Physics, University College Cork, Cork, T12 YN60, Ireland*

Exploring the power and phase profiles of spin waves not only enhances our fundamental understanding of magnetic materials but also opens up avenues for energy-efficient technologies such as, spintronics, magnonics, and reservoir computing. Here, we present the power-phase distributions and their tuneability of a surface acoustic wave (SAW) driven "Magnon Microwave Antenna" (MMA), comprised of patterned arrays of magnetostrictive nanomagnets embedded in piezoelectric heterostructures. The MMA generates tunable microwave frequencies without external bias fields, thanks to phonon-magnon coupling, producing multimode microwave frequencies with nonvolatile spin textures. A comprehensive static magnetic study elucidates the crucial role of the demagnetization energy distribution rather than its overall magnitude in magnetization reversal processes. Additionally, functional tunability could be achieved through amplitude-dependent training using various combinations of nanowire and nanodot dimensions, topologies, material properties, and array configurations. The non-volatile nature of the spin textures generated in the MMA, under bias field free condition is promising for energy-efficient logic and low-power computing applications. Thus this work introduces a novel alternative approach, paving the way to utilize these MMAs for on-chip reservoir computing, where amplitude varies at the operating frequency.

I. INTRODUCTION

A spin wave (SW) is a collective excitation of the magnetic moments in a magnetic material, which is when quantised is referred as magnon [1, 2]. Such SWs are often used to transfer and process information in a manner similar to electromagnetic (EM) waves, as used in electronic devices. Generally, the power of a SW is related to the number of spins involved in the excitation and their collective behaviour. The phase of a SW, on the other hand, refers to the relative timing or position of the spins within the wave. The power–phase relation of SWs, denoting the connection between intensity and phase, unveils essential insights into the nuanced characteristics of these propagating waves. The correlation between power and phase is pivotal, as understanding the interdependence between power and phase is integral to deciphering the intricate dynamic behavior of SWs from fundamental perspective, ultimately guiding the design and optimization in terms of their application in cutting-edge technologies.

Notably, the modern era has developed a great interest in microwave-based technologies due to the emergence of the Internet of Things (IoT) devices that combine lower power consumption, strong signal amplitude, and good frequency stability. However, traditional voltage controlled oscillators (VCOs) usually require a significant amount of electrical power to carry out their operations. Previously, spin torque oscillators (STO) have been explored as a potential source of microwaves due to their high tunability and small chip size compared to existing VCOs [3, 4]. However, they suffered from a weak output signal, which led to the investigation of an array of synchronized phase-locking STOs as a solution to this problem. Nevertheless, these phase-locking STOs have an extremely short synchronization time, and also synchronizing itself becomes a significant challenge in practical applications, limiting their use for cutting-edge IoT applications. Moreover, controlling the STOs requires an external bias in the form of an electric or magnetic field [5, 6], prompting the need for bias field free cutting-edge devices, as a solution. SW based devices could be a potential solution in circumventing those issues, as such devices deal with spins of electrons [7] and the generated effective internal magnetic field.

A SW based nanomagnetic antenna is an integrated magnetic device that is constituted of patterned magnetostrictive (MS) materials on the piezoelectric (PE) substrate having dimensions in the order of tens of nanometers, potentially which could be used in a variety of applications, including ultra-compact transceivers, sensing and microwave applications etc. While such spin wave/magnon based nano-patterned magnetic antenna is operated in the microwave frequency range is known as "Magnon Microwave Antenna" (MMA) [8], utilizing the interaction between the phonons (generated from piezoelectric layer), magnon (originated from magnetic nanopatterns) and photons EM radiation in the space). It is noted that the phonons, magnons and photons are the quantized acoustic waves, SWs and EM waves, respectively. It is worth noting here the fundamental difference between an antenna and oscillator. For instance, an oscillator works as a dc-to-ac converter, where the input is fed by a dc power source and the output provides a converted ac signal, which is not radiated in space, but generated over a load (like a resistor). An antenna, on the other hand, is excited by an ac signal and radiates that ac signal into the surrounding medium [9].

When the MMA is subjected to an alternating electric field, a sinusoidal stress is generated in the PE layer, that travels along the surface of the PE substrate as a surface acoustic wave (SAW). The SAW is then transferred to the patterned MS NWs, which in turn excites the magnetization in the same to form collective SW excitations [10]. The resulting SWs further radiate the EM waves (photons) at the

* arindam.samanta@tyndall.ie
† saibal.roy@tyndall.ie

SAW frequency as the SWs get coupled to the EM radiative modes via magnon-photon coupling and which can be used to transfer information and energy in the nanoscale regime [8, 9]. It is worth mentioning that moments of MS NWs experience effective internal magnetic field due to the dipolar interaction and exchange interaction, which further shows a sustained magnetization precession. Moreover, nanomagnetic antennas have several advantages over the conventional electrical antennas, including high miniaturization, improved directivity, higher magnetic confinement, and lower power consumption [11]. The small size and high efficiency of such nanomagnetic antennas make them well-suited for use in wide range of applications, including communication systems, sensing systems, microwave based technologies, etc. [12].

In the process of microwave generation through MMA, it is identified in our previous work that there are creation and annihilation of domains within the consisting magnetostrictive nanowires/nanodots on the piezoelectric substrate [8]. The creation of domain, i.e., the multi-domain state is generated due to the application of transverse stress along the y-direction. Following that, when SAW is applied along the longitudinal direction (i.e., x-axis), the multi-domain state gets converted into a single domain state, i.e., the corresponding domains are annihilated. However, such an important journey towards generating microwaves though the creation and annhilation of domains empowered by phonon-magnon coupling has overlooked the correlation of magnonic power profile and phase distributions at the operating frequency, which are extremely crucial for evaluating the performance of magnetic materials and devices, and accordingly to optimize their design for specific magnon based applications. In the digital modern era, lately developed artificial intelligence (AI), and machine learning (ML) processes have transformed data processing with the focus on enhancing speed, performance, miniaturization, and energy efficiency [13–16].

In that context, the most significant hurdle in the realm of modern electronics revolves around the pursuit of energy-efficient solutions tailored for information processing endeavors, particularly while dealing with noisy or incomplete dataset(s) [13]. On such occasion, a potential promising avenue is the adoption of physical reservoir computing [14], a novel approach that capitalizes on the inherent nonlinearity and recurrence of dynamical systems, colloquially referred to as the reservoir, bypassing the need for extensive training. This innovative paradigm not only challenges the conventional computing norms but also beckons towards a future where the intricacies of dynamical systems become the backbone of efficient and powerful information processing.

Here, this manuscript investigates into the complex linear as well as non-linear dynamics of SWs and their associated power and phase distribution within a SAW driven phonon-magnon coupling based MMA. Furthermore, it describes the possibility to tune the domains vis-à-vis corresponding power-phase distributions in presence of an external bias magnetic field, manipulating NWs/NDs dimensions and array configurations, which in turns offers an opportunity to utilize these MMA for reservoir computing as elucidated subsequently.

II. RESULTS AND DISCUSSION

In nanowire or nanodot arrays, the interplay between magnetostriction, exchange, and dipolar interactions leads to complex and tunable magnetization dynamics. For instance, magnetostriction couples SAWs from the piezoelectric layer (e.g., $LiNbO_3$) with magnetostrictive nanomagnets (FeGa), inducing strain that alters magnetic anisotropy and excites spin waves i.e., magnons. Such magnetostriction efficiently converts acoustic energy into tunable spin waves, enabling synchronization and asynchronization of magnetization dynamics without the need for external magnetic fields. This mechanism provides the foundation for controlling spin-wave behavior in a bias-free environment. Additionally, the exchange interaction, a short-range force between adjacent magnetic moments, aligns spins and stabilizes magnetic domains in nanostructures. In closely spaced arrays, such as nanowires or nanodots, the exchange interaction ensures strong coupling between neighboring magnetic moments, which impacts the uniformity of spin-wave modes across the structure. Such uniformity is key to achieving stable and coherent magnetization oscillations across the entire system. Furthermore, The dipolar interaction, a long-range force, aligns magnetic moments into domains over larger distances, enabling collective behavior like the synchronization of magnetization oscillations and frequency locking of spin waves. This is crucial for coordinated spin-wave dynamics, which is vital for high-dimensional signal processing in reservoir computing.

A. SAW Analysis: COMSOL Simulation

In this work, first, we have designed and simulated some typical nano-patterned MMA in COMSOL Multiphysics® [17] to obtain the SAW frequency, which we have further used as input in micromagnetic simulation with MuMax^3 [18]. The schematic of the MMA as shown in Fig. 1(a) is composed of FeGa MS NWs shaped in particular patterns onto a PE $LiNbO_3$ substrate. To carry out the design and simulations, the structural mechanics module of COMSOL Multiphysics is used in conjunction with the AC/DC module. This combination enabled both the piezoelectric effect and magnetostriction physics interfaces. The SAW frequency, estimated from the S_{11} parameter, is 550.75 MHz, which propagates along the longitudinal directions. The penetration depth of the surface acoustic wave (SAW) is 45 nm, as shown in Fig. 1(c), and therefore, the nanowire/nanodots thickness is restricted below 45 nm to ensure that the entire stress has been transferred into the nanowires/nanodots properly [8, 9].

We now calculate the amount of power that is coupled to the SAW, which could be further utilized in estimation of the stress generated upon launching of SAW. In order to do that, we have considered the similar approach by De et al. [10] and Drobitch et al. [19]. Here, the S_{11} parameter in Figure 1(b) has been calculated considering an ideal scenario, i.e., any loss from the substrate has been neglected, that estimates the reflection coefficient of the system. The S_{11} value of ≈ -7.56 dB gives the reflection coefficient of the system as

≈ 0.175. Here, in the simulation, the input power (P_I) is 10×10^{-3} W. Therefore, the power coupled into the SAW is $P_C = (1-r) \cdot P_I \approx 8.25 \times 10^{-3}$ W. The velocity of acoustic waves in $LiNbO_3$ typically ranges from 3 to 6 km/s [8, 9]. For our calculations, we will use an approximate average velocity of 5.5 km/s. This assumption leads to the maximum penetration depth, λ_{max} of 10 μm, considering operating frequency at ~550 MHz. Therefore, the SAW crosssectional area becomes, $A_{max} = \lambda_{max}$ times width of the electrode $= 1 \times 10^{-11}$ m^2. Hence, the effective power coupled with the SAW is, $P_{C,max} = P_C / A_{max} = 8.25 \times 10^8$ W/m^2.

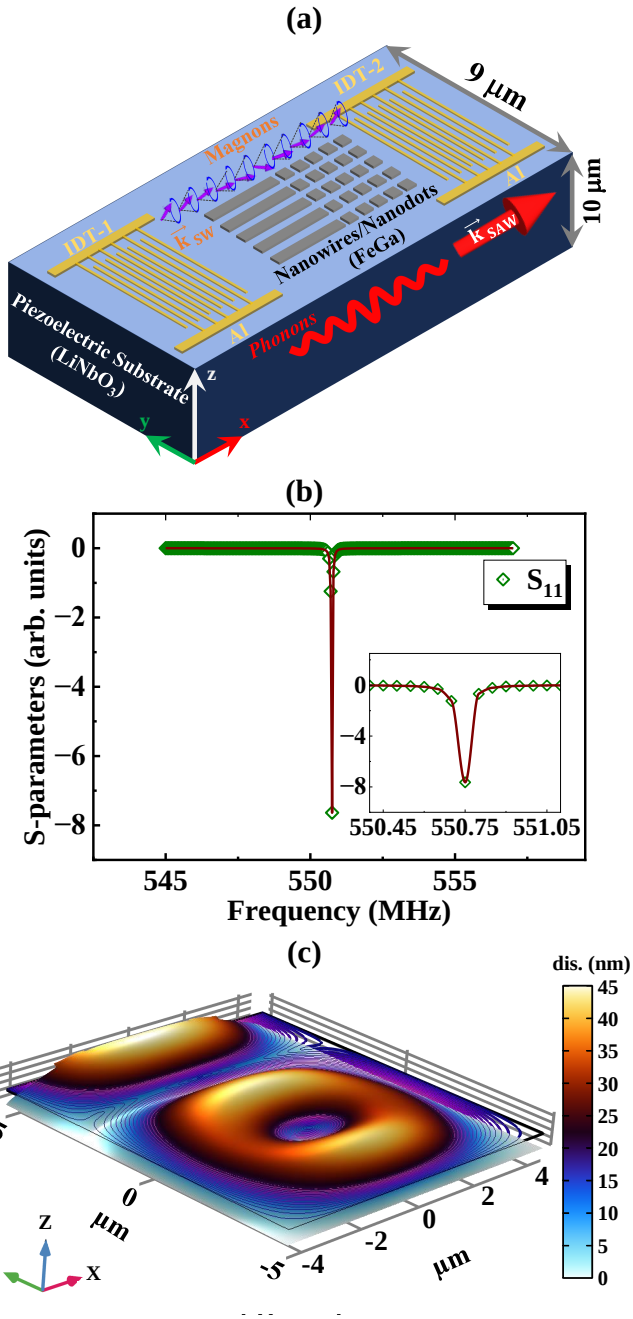


FIG. 1. (a) 3D schematic of magnon microwave antenna (MMA) with magnetostrictive (FeGa) nanowires (NWs). $\vec{k}_{SAW}$ and $\vec{k}_{SW}$ are the wave vectors associated with the SAW and the SW, respectively. Here, the width and thickness of the piezoelectric substrate ($LiNbO_3$) are 9 μm and 10 μm and that of the interdigitated transducer electrodes [*IDT-1* and *IDT-2* in the schematic] of *Al* (stands for Aluminum) are 1 μm and thickness 100 nm, respectively. (b) S_{11} parameter confirms the resonance frequency of SAW at 550.75 MHz. (c) Deformed shape plot at the resonance SAW mode estimates the penetration depth of 45 nm.

B. Stress and Anisotropy Calculation

The power coupled to the SAW generates stress in the magnetostrictive nanowires/nanodots, which in turn alters their magnetic anisotropy. The stress (σ_{stress}) can be estimated from the coupled power as follows: $\sigma_{stress} = \sqrt{2 \cdot P_{C,max} \cdot Z_{max}}$, where Z_{max} is characteristic acoustic impedance calculated as: $Z_{max} = \sqrt{C_{11} \cdot \rho}$, where $C_{11} = 202.897 \times 10^9$ Pa is the first diagonal element of the elasticity tensor, and $\rho = 4.7 \times 10^6$ g/m^3 is the density of the $LiNbO_3$ substrate. This results in $Z_{max} = 9.786 \times 10^8$ N$\cdot$S/m^3 and the effective stress acting on the magnetostrictive material of $\sigma_{stress} = 1.27 \times 10^9$ Pa.

This stress due to launching of the SAW alters the magnetic anisotropy (K_{eff}) of the nanowires, defined as: $K_{stress} = -\frac{3}{2} \lambda_S \cdot \sigma_{stress} \cdot \sin(2\pi f_0 t)$ [8, 9], where $\lambda_S = 400$ ppm is saturation magnetostriction constant of FeGa [20, 21], and $f_0 = 550$ MHz is the resonance frequency of SAW. Therefore, the total effective anisotropy becomes $K_{eff} = K_{u1,i} + K_{stress}$, where K_{u1} is the anisotropy. This anisotropy affects the internal magnetic field with an amplitude of $\frac{\lambda \cdot \sigma_{stress}}{\mu_0 \cdot M_S}$, contributing to the magnetization dynamics of the system.

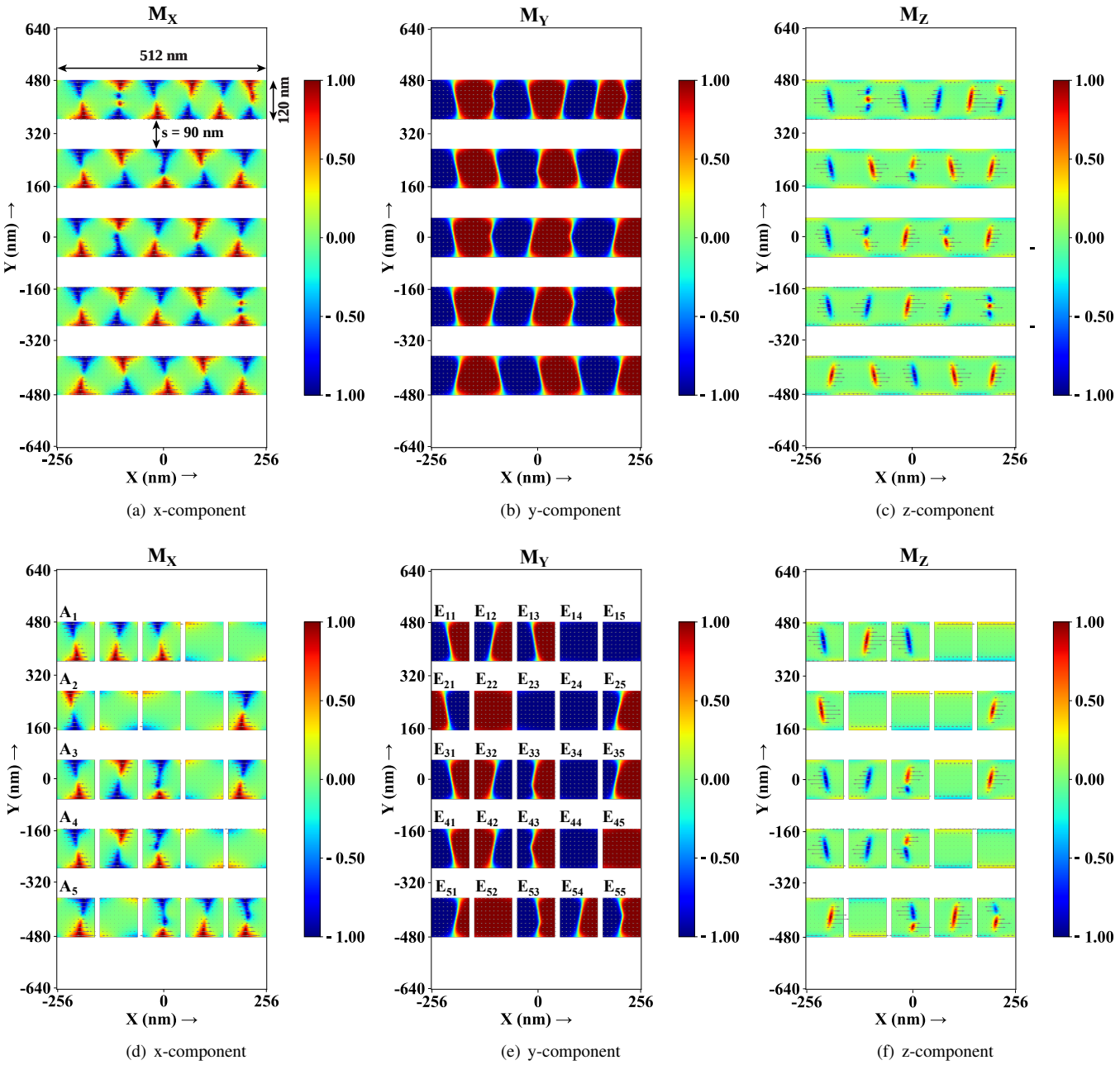
C. Spin Wave Analysis: MuMax^3 Simulation

The micromagnetic simulations using MuMax^3 [18] have been performed considering the calculated stress and anisotropy values to model the spin wave dynamics. The nanowires (NWs)/nanodots (NDs) were discretized into the cell sizes of $2 \times 2.5 \times 2.5$ nm^3. MuMax^3 solves the Landau-Lifshitz-Gilbert (LLG) equation, which governs the magnetization dynamics under the effective magnetic fields (H_{eff}) generated due to shape anisotropy, dipole coupling, and strain:

$$\frac{\partial \vec{M}}{\partial t} = |\gamma| \vec{M} \times H_{eff} + \frac{\alpha}{M_S} \left[\vec{M} \times \frac{\partial \vec{M}}{\partial t} \right] \quad (1)$$

$$H_{eff} = -\frac{1}{\mu_0} \cdot \left[\frac{\partial E}{\partial \vec{M}} \right] \quad (2)$$

It determines the macro-spin configuration at every coordinate point within the NWs/NDs and it produces the vector files containing the magnetization distribution over the simulating magnetic object. The following material parameters of FeGa [20], saturation magnetization $M_S = 1.32$ MA/m, exchange stiffness constant $A_{ex} = 16$ pJ/m, initial exchange



(a) x-component (b) y-component (c) z-component

(d) x-component (e) y-component (f) z-component

FIG. 2. For 's' = 90 nm configuration, (a) x–, (b) y– and (c) z– components of the multidomain state in presence of the transverse stress and for nanodots that are in (d), (e) and (f), respectively. Length and width of the individual nanowires remain constant throughout the study at 512 nm and 120 nm, respectively. For the nanodots, while the separation along y-axis is 90 nm that along the x-axis is 14 nm. Here, A_1 to A_5 denote the nanodot array while the E_{ij} denotes the individual nanodot elements for i^{th} row and j^{th} column, where $i, j = 5$.

anisotropy constant $K_{u1,i} = 0\ J/m^3$, before applying external stress (σ_{stress}) are used in the simulation. We note that the effective internal magnetic fields is generated due to the effect of the shape anisotropy, dipole coupling and strain. This micromagnetic modelling of strain-mediated structures have been conducted at 0K to neglect switching defects, a widely used method [8, 22].

Here, the cell size lies below the exchange length ($l_{ex} = \sqrt{\frac{2A_{ex}}{\mu_0 M_S^2}} \approx 3.82$ nm), which further ensures the inclusion of all of the exchange interactions [23]. The simulations were performed with typical NW dimensions of $512 \times 120 \times 40$ nm^3 (length × width × thickness) and with varying separation values (denoted as 's') ranging from 20 nm to 160 nm. The simulations provided the magnetization distributions and the spin wave dynamics within the nanostructures.

A typical example with 's' = 90 nm separated nanowire

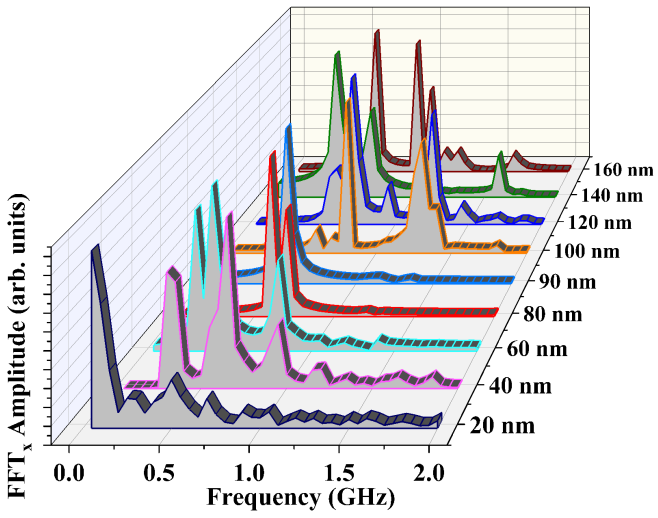


FIG. 3. Variation of power distribution obtained from fast Fourier Transformation (FFT) of magnetization as a function of NW spacing.

array/nanodots matrix is shown in Figure 2(a)/(b)/(c) and (d)/(e)/(f), respectively. The spatial distributions of the x–, y–, z– components reveal different domain configuration along the respective directions. The multi-domain state predominantly forms along the y– direction, where up (brown) and down (blue) spins are separated with the domain walls, as expected given the application of transverse stress along the y– direction. On the other hand, the x– and z– components primarily consist of in-plane spins (greens region with zero magnitude), while they are separated by either alternate down (blue) and up (red) spins along the edges (for x– directions) or by alternate up (red) and down (blue) spins within the nanowires (for z– directions), respectively. However, the spatial distributions for the nanodot matrix exhibit a drastic variation in domain configuration compared to that of the continuous nanowires, as shown in Fig 2(d)/(e)/(f).

Let us consider the domains of the x– component (for the dot-matrix). The first three elements (E_{1j}, $j = 1-3$) of the A_1 array of the matrix have a similar domain configuration with in-plane spins edged by down (blue) and up (brown) spins on the top and bottom sides, while the last two consist mostly of in-plane spins. Similar domain configurations are formed for the other arrays as well. The M_Z domain structure also mostly formed with consistent in-plane spins, where some of the elements are centered by either up spins or down spins. However, the multidomain state with up/down spins separated by domain wall also forms for the M_Y component along the y– direction. Interestingly, there are some elements which are dominated with either up spin or down spins. For example, elements, E_{14}, E_{15}, E_{23}, E_{24}, E_{34}, E_{44} are strongly dominated by down spin configuration, while elements, E_{22}, E_{45} and E_{52} are strongly dominated by up spin configuration; which might be the one of the reasons behind such complex magnetization oscillations observed along the x direction [as shown later in Figure 4(a)].

In case of 's' = 20 nm configuration, a dominant peak is observed at a 50 MHz frequency as depicted in Fig. 3(a). This observation implies inadequate coupling of the Surface Acoustic Wave (SAW) at this frequency with the spin waves. The configurations for 's' = 40 nm, 60 nm, 140 nm, and 160 nm display three distinct peaks. Specifically, for 's' = 40 nm, the central peak is at 650 MHz, accompanied by two sub-bands at 300 MHz and 950 MHz. Similarly, 's' = 60 nm is centered at 400 MHz with sub-bands at 300 MHz and 800 MHz. Moving on, 's' = 140 nm dominates at 500 MHz, featuring two upper sub-bands at 700 MHz and 1600 MHz, while 's' = 160 nm is centered at 900 MHz with sub-bands at 600 MHz and 1000 MHz. Among the other configurations with two peaks, 's' = 80 nm has peaks at 600 MHz and 700 MHz, 's' = 100 nm has peaks at 800 MHz and 1300 MHz, and 's' = 120 nm exhibits peaks at 700 MHz and 1250 MHz. Notably, the 's' = 90 nm configuration stands alone at 550 MHz without any sub-bands, indicating effective coupling of the SAW with the generated spin waves. Consequently, this 's' = 90 nm configuration yields an optimum synchronized output with sustained oscillation [8].

For all geometrical configurations, the exchange energy of the initial random magnetization state (not shown here) is three order of magnitude greater than the multi-domain state and the single domain state, which is expected as in random distribution the neighboring moments within each NW are coupled randomly through strong exchange interaction. Since there is no external magnetic field applied, the Zeeman energy is zero and hence not considered. Moreover, the magnetic dipoles tend to align in a way that minimizes the overall energy of the system. This interaction contributes to the stabilization of the aligned magnetic moments within a domain. With the introduction of a Surface Acoustic Wave (SAW) in the longitudinal direction (x– direction here), one can consider the magnetic interconnection between the neighbouring NWs as a parallel combination through dipolar coupling, akin to how electrical Spin Transfer Oscillators (STOs) function through resistive connection. It's crucial to emphasize the vital roles played by demagnetization energy and exchange energy in maintaining stable magnetization oscillations. Therefore, finding a suitable equilibrium or a trade off between these energy components is imperative for these systems [8].

Each of the individual nanowire (five here) in the MMA is observed almost in single domain state (as shown in Figure 2) for the s = 90 nm configuration while the other configurations (s = 20 nm to 160 nm, other than the 90 nm configuration; not shown here) all the nanowires failed to form such single domain state like the earlier. Throughout the study here, each of the studied magnetostrictive nanowires has a high aspect ratio (AR) of ~ 4.2, defined as length:width (512 nm:120 nm), which we kept constant. We note that the demagnetization energy plays an important role in stabilizing the domains [1, 24], which is the case in our study due to such high aspect ratio. Therefore, the tiny spacing between the neighbouring nanowires (s = 20 nm to 160 nm) comes into the picture and determines the domain configuration. Each of the nanowires would experience the exchange energy due to small separation between them, and hence, the demagnetization energy or the

dipole interaction (due to the high aspect ratio) would compete with the exchange energy. As the single domain in each of the nanowires has its own directions, it is imperative to check the magnetization oscillations for each of the nanowires, as elucidated later.

Figure 4(a) shows the magnetization oscillations of individual NWs (where, each of the NWs are labelled as 1-5 in order from top to bottom as shown in Figure 2(a)) along x direction. We observe that each of the NW oscillates in their own way, however, they are synchronized to the overall magnetization. Here, [in Figure 4(a)], only the magnetization oscillation of the NW-4 is similar to the overall magnetization oscillations of the system, i.e., synchronized properly with the input. In this case, the relationship between the input (surface acoustic waves) and the output (magnetization oscillations of overall system/NW-4) follows almost a linear pattern.

On the other hand, the other nanowires (namely, NW-1, 2, 3 & 5) show significantly different magnetization oscillations. Their amplitudes increase or decrease in a random manner, signifying the possibility of frequency mixing, i.e., an interaction between different frequencies that generates new frequencies not present in the original input. Such behaviour of the system hints towards the generation of nonlinear dynamics within each of the nanowires and that nonlinear spin wave behaviour may introduce complexities such as higher harmonics, different mode coupling, and frequency mixing, which might be beneficial for reservoir computing as described later. Since the NW-4 is synchronized with the output possibility of its detection of the task/signal will be the least probable, whereas, the possibility of its detection in the NW-3 might be the highest.

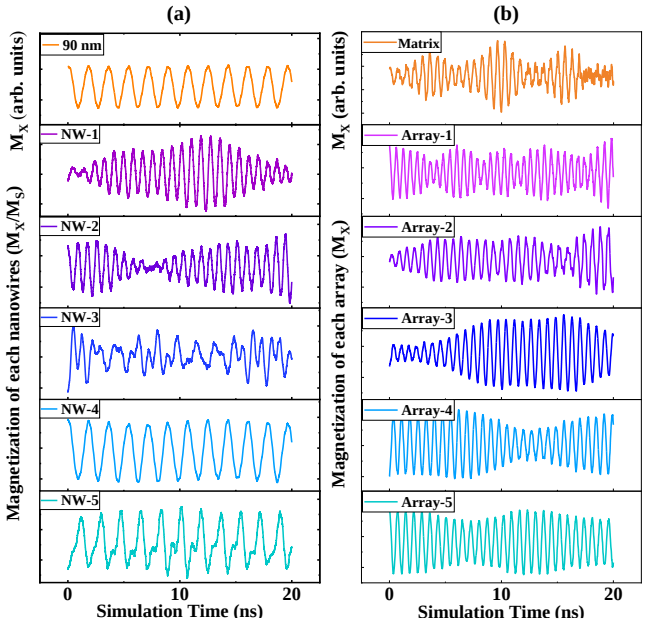
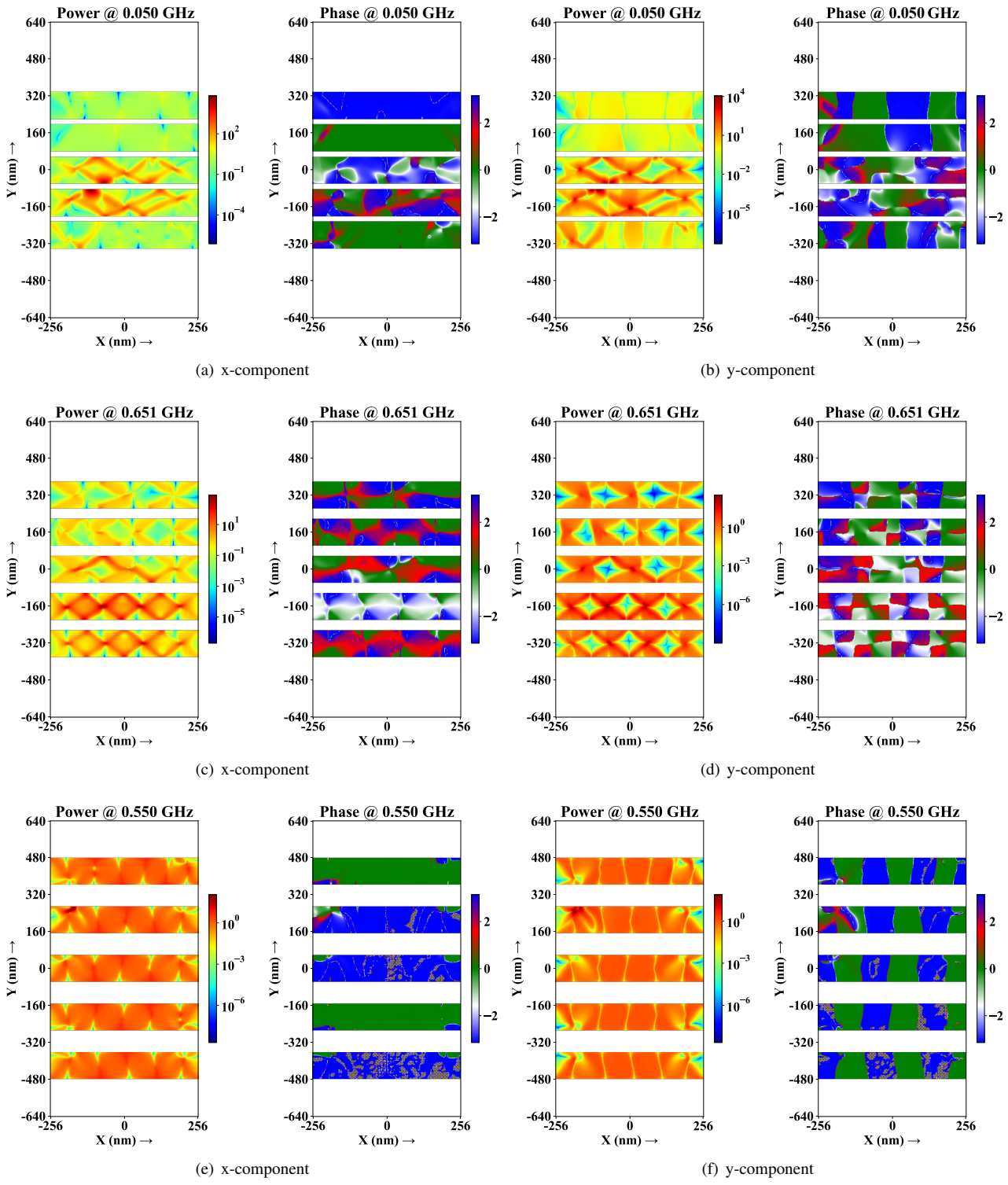


FIG. 4. The (a) M_X component of each nanowire for 90 nm configuration, respectively while, the top row highlights the overall magnetization of the whole system. For the nanodot array, the (b) M_X component of each array, respectively while, the top row depicts the overall magnetization responses arising from the whole system.

A similar scenario is observed for the nanodot array. The overall magnetization oscillation for nanodots even does not synchronize with that of the individual arrays, as shown in Figure 4(b). Therefore, it might be optimal for probabilistic computing. While the proposed MMA shows potential for such probabilistic computing, a detailed explanation from this perspective is beyond the scope of the present study. At the 20 nm and 40 nm configurations, the dominance of intrinsic shape anisotropy and the strength of magnetostatic interaction is notable (as explained later in section II E). In these cases, the overall demagnetization energy surpasses the exchange energy, hindering synchronization with the launched surface acoustic wave (SAW) frequency. Consequently, incoherent magnetization precession, intrinsic to the array, occurs within the nanomagnets. This leads to power distribution at both lower and higher frequencies, potentially influenced by the array geometry [10].

It is important to note that the selection of nanowire and nanodot arrays is crucial for tuning magnetization behavior. Nanowires posses enhanced uniaxial anisotropy and dipolar interactions due to their elongated geometry. This leads to distinct domain formation and longitudinal spin-wave propagation, which is further influenced by the separation of nanowires. On the other hand, nanodots have more localized domain configurations due to their smaller sizes. The variation of magnetization within the nanodots is influenced by exchange and dipolar interactions. In both the cases, the number and length of arrays affect the synchronization of spin waves, with longer arrays increasing dipolar coupling for frequency locking and finer control of power-phase distributions, important for reservoir computing applications, as explained in the later sections.

In the case of the 20 nm configuration, with only one peak, it can be inferred that no nanowires are synchronized with each other. The x-component of magnon power distribution [refer to Figure 5(a)] illustrates that the highest power is localized predominantly between NW-3 and NW-4 at two points (dark red region), indicating non-uniform distribution. Notably, systems tend to stay in the lowest energy state, and the complex canted power profile in NW-3 and NW-4 suggests that, while traveling longitudinally, the magnon path bifurcates towards the edge of the nanowire (potentially due to the system's exchange energy) and reunites, returning from the edge to the middle of the nanowire (possibly due to strong dipolar interaction) to minimize the system's energy. Consequently, the relatively higher power (orange region) in NW-3 and NW-4 follows a zigzag path, forming a tetrahedron shape (henceforth mentioned as, diamond shape), where the lower power is surrounded by higher power. Other nanowires exhibit a moderate power distribution (green-yellow region) with some lower edges (sharp blue lines in NW-1, 2, and 5) between them, highlighting complexity in the phase profile. In general, the propagating spin waves (here the red region; travelling longitudinally) involve a coherent movement of the phase of the spin precession across space, while standing spin waves (here green-yellow region; almost constant) involve a stationary pattern of spin precession.



(a) x-component (b) y-component

(c) x-component (d) y-component

(e) x-component (f) y-component

FIG. 5. Magnon power profile and phase distribution for 's'=20 nm in (a)/(b) showing desynchronized states, for 40 nm configurations with partially synchronized states in (c)/(d), and for 's' = 90 nm revealing the synchronized state with uniform distribution in (e)/(f), respectively.

NW-1 exhibits a phase distribution of 180° ($\equiv \pi$ rad), while NW-2 and NW-5 have a 0° phase. This suggests that NW-2 is in phase with the input Surface Acoustic Wave (SAW), while NW-1 is out of phase. A closer examination reveals alternating sharp blue edges with changes in direction. Considering the y– direction, it is horizontally divided into two parts, i.e., the quantization number is $\mathrm{n_y} = 2$. The blue region, representing the lowest magnon power, implies an attempt

to distribute energy associated with magnon power among neighboring nanowires. Consequently, a zigzag pattern is observed, possibly due to the coexistence of propagating spin waves and standing spin waves (as explained earlier) preventing synchronization between neighboring nanowires along the longitudinal direction. On the contrary, the y-component in Figure 5(b) displays complex quantization. For example, NW-1 and NW-2 are vertically divided with $n_x = 5$ and 3, respectively, while NW-3 and NW-4 are horizontally divided with quantization number $n_y = 2$. Notably, NW-5 first follows a zigzag path and then divides horizontally with quantization number $n_x = 3$. The phase distribution of the y-component for NW-1 and NW-2 does not exhibit clear synchronization, as they are well-separated with π rad and 0 rad. However, unlike the x-component, NW-1 and NW-2 are in the same phase. Similar behavior is observed for NW-5 as well. However, NW-3 and NW-4 show a random phase distribution.

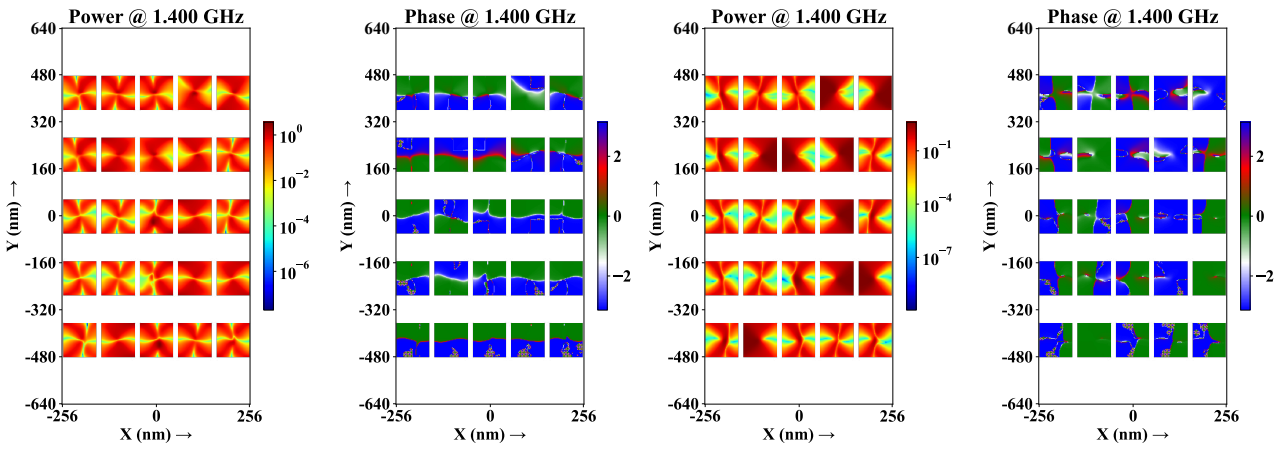
In the x-component, NW-3 exhibits a tiny region with no phase (green with 0 rad) surrounded by a $-\pi/2$ rad phase region, while in NW-4, it is a $\pi/2$ phase region. A similar pattern is observed for the y-component. Since the gap in both cases of phase distribution is extremely small, it could be considered that those positions in the two NWs (NW-3 and NW-4) are synchronized. However, such synchronization is challenging to control, as the spin wave in this case is mainly influenced by the array geometry.

In the case of the 40 nm configuration, there are three peaks in the corresponding spectrum, indicating that at least two nanowires (NWs) are synchronized along the x direction simultaneously, as observed in Figure 5(c). For instance, NW-4 and NW-5 appear to be synchronized, although there is a noticeable difference in the amplitude of power between them. Compared to the 20 nm configuration, the power of the central peak is lower, signifying that the exchange energy dominates over the demagnetizing energy of the system this time (as evidenced in Table S1). Consequently, the launching of Surface Acoustic Wave (SAW) gives rise to new extrinsic modes. The associated phase and power profiles of the spin waves of the M_X and M_Y components, at the central peak frequency (i.e., 0.65 GHz) are shown in Figure 5(c) and 5(d), respectively (obtained after post-processing of the magnetization data with python). For NW-1 and 2, the power is distributed diagonally (towards higher region) from its respective origin (lower region). The power in NW-3 traverses along the zigzag path (and a weak diamond shape distribution), possible due to the competition between exchange energy and the demagnetizing energy. The NW-4 and 5 show previously explained diamond shape distribution for the x-component.

In this studied nanowire system, the quantization numbers provide insight into the distribution of power along different directions. Notably, $n_y = 2$ suggests a vertical quantization of power, while varying values of n_x along the horizontal direction (e.g., $n_x = 4$ for NW-1 and NW-2, $n_x = 5$ for NW-4 and NW-5) indicate different modes of power confinement. The complexity observed in NW-3, where n_x is unidentifiable due to a complex pattern, hints at intricate power distribution characteristics. The phase profile at a specific frequency reveals a complex propagation mode of spin waves, indicative of collective spin excitations. Particularly, at a 40 nm configuration, the power in the spin wave is not confined to a single frequency, suggesting a broader distribution across frequencies. This multifaceted analysis underscores the nuanced behavior of spin waves in nanowires, influenced by their geometry and material properties, with implications for diverse frequency modes and intricate power distribution patterns.

Now, we discuss the power profile and phase distribution for 's' = 90 nm configuration along x– and y– directions, as shown in Figure 5(e)/5(f), which reveals that the power at 0.55 GHz is evenly distributed between the five nanowires. Since the power shows almost uniform distribution the magnon power is concentrated at this particular frequency only and as a result, a synchronized single peak is observed in the FFT power spectra, as shown in Fig. Fig. 3(a). A closure insight reveals that the power suffers a tiny edge effect (green-yellow region, i.e., comparatively the lower power region) in its magnon power distribution [Figure 5(e)], which allows the spin wave to travel throughout the nanowire along the longitudinal direction. Since all the nanowires are synchronized no diamond shape is observed. Accordingly, both the quantization number, n_x and n_y become 1 for this case. The phase distribution shows that the NW-1 and 2 have π phase difference while the NW-2 and 3 seem to be mostly in same phase. Similarly, NW-3 and 5 have π phase difference compared to NW-4. As explained earlier, there exist local synchronization in phase for some of the positions in the individual nanowires (e.g., NW-2, 3 and 5). Interestingly, the uniform power distribution throughout the five nanowire for the y-component as shown in the Figure 5(f) shows quantization number $n_y = 1$ and $n_x = 5$. This time the edge effect appears on the extreme left and right of the each of the nanowires. Each of the nanowires are in phase along the y-direction. However, in each of the nanowires there is π phase difference between the adjacent portions.

Now, we consider the power distributions and phase profiles of the arrays of the nanodot matrix, as shown in Figure 6 where each of the elements is separated horizontally by 14 nm distance and vertically by the optimum separation, 90 nm, at which we obtained sustained synchronized oscillations in the nanowires. Most of the magnon power (red/brown) is distributed evenly throughout each of the elements of the nanodot matrix, as shown in Figure 6(a). However, a closure insight reveals that comparatively lower magnon power (either green/yellow or yellow-green mixture) edged along each direction (top, right, bottom and left) of the nanodots creates an inverse tetrahedron structure. Therefore, they do not have such straight quantization numbers, n_x or n_y. However, some of the elements, e.g., E_{14}, E_{15}, E_{22}, E_{23}, E_{24}, E_{34}, E_{44}, E_{45} and E_{52} form a mirrored conical pattern lacking comparatively lower powers along the top and bottom directions. On the other hand, the phase profile exhibits significant interesting distribution. For instance, the top (green, i.e., 0 phase) and bottom (blue, π phase) halves of the $E_{1j}, j = 1-3$ elements are in same phase while E_{14} and E_{15} elements are inversely synchronized separated by



(a) x-component (b) y-component

FIG. 6. Magnon power profiles and phase distribution for the array configuration showing complex synchronization state within the nanoelements of the matrix.

tiny phase either $\pi/2$ (red) or $-\pi/2$ (white) phases. Similar kind of synchronization is observed for the other arrays due to the appearance of such $\pi/2$ (red)/$-\pi/2$ (white) separation between the green (0 phase) or blue (π phase).

Similar kind of almost evenly distributed magnon power is observed for the y– component as well, as shown in Figure 6(b). Instead of the lower power distribution along the four directions, this time, the magnon power is almost equally halved in the right and left directions only, resulting into the quantization number, $n_x = 2$ for each element and accordingly the formation of the conical shapes. However, interestingly, those elements which lack lower magnon power distributions along the x– direction on the top and bottom parts, i.e., the elements E_{14}, E_{15}, E_{22}, E_{23}, E_{24}, E_{34}, E_{44}, E_{45} and E_{52} exhibit a comparatively higher magnon power distribution in any one half of the elements. It is interesting to note that a higher value of n_x/n_y for the phase spectra results in a greater displacement of magnon intensity toward the periphery of the nanowire or nanodots. This phenomenon can be intuitively explained by the decrease in exchange energy. By maintaining an expansive region surrounding the circular core (might be a 'vortex') with the comparatively lower amplitude, a pronounced deviation of neighbouring spins in close proximity to the vortex core is mitigated, consequently leading to an overall reduction in the total energy [25].

An intriguing observation is that the spin waves observed here are not propagating; instead, they are localized at the centre of each element. This localization might be attributed to the formation of vortices, favoured by the strong demagnetization energy characteristic of the multi-domain state. As the nanowires are patterned into nanodots, the demagnetization energy strongly dominates over the exchange energy of the multi-domain state. While the exchange energy of the single domain state surpasses the demagnetization energy, it proves insufficient to induce the movement of the spin wave. Consequently, the stationary nature of the spin wave is observed, primarily influenced by the matrix (nanodots) geometry. Power and phase profile of the spin wave show complicated spin wave distribution, i.e., the spin wave has propagation mode as well as standing mode. The propagating spin waves are longitudinally traversing across the continuous nanowires. Note that, instead of following an undeviating path, it follows a zigzag track. Interestingly, along with such propagating mode, localized edge modes as well as bullet modes appeared/co-existed on such zigzag spin wave track (Figure 6(a)). The edge mode appears alternatively at certain intervals, however, it fails to last throughout the cross section, i,e., it vanishes within the middle of the nanowires. In some cases, they formed bullet mode in the middle of the nanowire. However, a closure observation of the power spectra on the other hand reveals that the intensity of the propagating spin wave is smaller compared to that of the edge/bullet modes.

The *Kittel* mode refers to the uniform precession of spins in a ferromagnetic material, often observed in systems where an external magnetic field is applied to tune or control its frequency [26]. However, the presence of an external field is not strictly required for the *Kittel* mode to exist. In fact, internal magnetic fields, such as demagnetizing fields and exchange interactions, can also sustain this uniform precession, especially in structured systems like the nano-patterned heterostructures studied here. In our case, the system relies on the internal effective magnetic field generated by the materials intrinsic properties, and the *Kittel* mode can still exist due to the internal anisotropy fields present in the nanostructures. In our system, spin precession is driven by the phonon-magnon coupling induced by surface acoustic waves (SAWs) rather than an external bias field, making this system particularly suitable for low-power applications. The aforementioned material and system properties, including the dipolar coupling field and demagnetizing energy, play a crucial role in defining the array parameters. Thus, the spin waves in these systems are often described as exhibiting intrinsic spin wave dynamics [10]. The spin waves generated are the result of the effective coupling between the launched SAW and the

generated SW. When observing frequencies other than the synchronized frequency (e.g., 550 MHz at 90 nm separation), they presumably depend more on other parameters such as demagnetizing energy and exchange energy [8–10] apart from phonon-magnon coupling. The competition between these energies plays a significant role in stabilizing the transition from an initial random magnetization state to a single domain state, and subsequently, in sustaining magnetization oscillations within the nanomagnet. This complex energy balance leads to the frequency locking state of the MMA, as explained in section II D.

D. Frequency Locking at Optimum Separation

Injection locked studies within the electrically tunable spin torque oscillators (STOs) are usually performed to measure the mutually synchronized response of STOs to an external radio-frequency (rf) signal. Typically, during the injection locking experiments, an rf current (I_{rf}) in addition to the optimised external bias electric current (I_{dc}) is passed through the coupled oscillators, where the frequency of the I_{rf} is fixed at the resonance frequency/peak frequency [27]. As mentioned earlier, the MMAs do not require any external bias alternating magnetic field, the working principle of the MMA differs compared to the aforementioned electrically tuneable STOs, accordingly giving rise to the occurrence of a different injection locking phenomena here; this could be ascribed as frequency locking. Recently, it is experimentally observed that the SAW frequency could be manipulated in the piezoelectric substrate/magnetostrictive nano-matrix heterostructure by applying an ultrashort laser pulse [28, 29], which necessarily modulates the precessional dynamics and accordingly the phonon-magnon coupling (SAW-SW interaction) [30]. We have considered to perform the frequency locking response study by adding an additional external sine pulse with different frequencies varied between $1-500$ GHz to the mutually synchronized frequency (i.e., 0.55 GHz) at the optimum configuration as shown in Figure 7. Following that, we have studied the discussed frequency locking states of the MMA configured with 90 nm configuration.

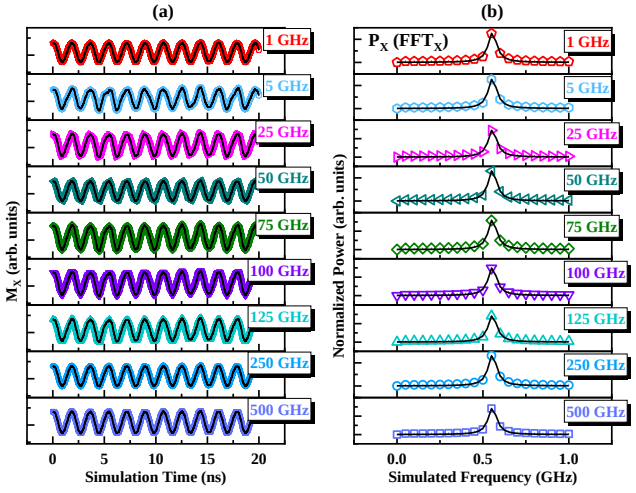


FIG. 7. (a) Magnetization dynamics along x– direction as a function of SAW frequency altered from 1 GHz to 500 GHz with included with 0.5 GHz parent frequency. The interdistance between the NWs remain constant at 90 nm to ensure sufficient exchange coupling and the dipolar interaction. (b) Power distribution of the frequency locked states as a function of frequency along x– direction.

The power distribution of the injection locked MMAs with different frequencies reveals an almost constant omnidirectional synchronized peak at ~ 0.55 GHz (f_{sync}) as depicted in Fig. 7(b). Hence, that f_{sync} peak might be intrinsic to the optimized geometry configuration [30, 31]. However, the power of the resonance frequencies follows the similar order, $P_X > P_Y > P_Z$, where, P_X, P_Y, P_Z are the obtained power of the resonance frequencies from the corresponding FFT of M_X, M_Y, M_Z, respectively (y and z components are not shown here). It is important to mention again that these MMA operates without the requirement of any external alternating bias magnetic field, which appears due to the absence of the fundamental Kittel mode in the MMA. Moreover, the array geometry parameters or the material parameters remain constant at the optimized 90 nm configuration, which might be responsible for establishing the frequency locking states between the neighbour nanowires in the MMA. Due to the frequency locking state the overall locking range gets enhanced (1-500 GHz) for the synchronized MMA as compared to the individual nanowire (0.5 GHz). Interestingly, auto-oscillations of the mutually synchronized states remain undisrupted over the whole frequency range. It is observed that over the longer time span the oscillations become more stable compared to that in the shorter span. Moreover, the power of the 50 ns oscillation (in every direction) increases significantly (see supplementary Figure S2). Since the MMA does not depend on any external alternating bias magnetic field, an increased power have been achieved independently. Therefore, our investigation offers a quite better energy efficient external bias field free performance over the conventional electronic devices. Moreover, when these structures emit the EM radiation into the surrounding space that could be captured by a horn antenna [9] and could be used in other applications as well, such as, energy harvesting. While the microwave applications is the outcome of the phonon-magnon interaction, the following photon emission (EM wave radiation) induced by phonon-magnon coupling would be beneficial for wireless energy harvesting due to abundance of Wi-Fi, mobile, and other communication signals.

It's noteworthy to highlight that the observed alteration in domain wall motion induced by Surface Acoustic Waves (SAW) holds promise for applications in wireless energy harvesting, particularly beneficial for power-intensive Internet of Things (IoT) devices [32]. Another crucial aspect of our investigation is the nonvolatility of the SAW-engineered single domain state (not shown here). The single domain nanomagnets maintain their state persistently until reset by either stress application or the application of a robust external magnetic field to revert to the initial multi-domain state. This nonvolatility presents opportunities for energy-efficient logic

applications and low-power computing [33], although this aspect is beyond the current scope of our study.

E. Static Magnetic Study

The preceding sections comprehensively elucidate the spin wave distribution/synchronization properties within the nanowires of the MMA under bias field-free conditions. However, investigating into its fundamental static properties in the presence of an external magnetic field is worthwhile, as it may uncover potential applications for other magnetoelectronic devices [34]. Moreover, it is well known that switching mechanism is very sensitive to the thickness to width ratio of the nanowires. While the thickness is ≤ 40 nm, previously for a patterned $Ni_{80}Fe_{20}$ nanowires, it was reported that coherent spin rotation dominates in the reversal mechanism [35]. So, we conducted additional simulations to analyze the hysteresis loop under two conditions: (i) before applying the SAW [Figure 8(a)-(d)] and (ii) after applying the SAW [Figure 8(e)-(h)]. All MMA configurations, namely, 20 nm, 90 nm, 160 nm, and the nanodot array, are initially saturated by applying an external magnetic field of magnitude 3 T ($\equiv 30000$ Oe). Subsequently, the hysteresis loops are simulated. We note that for the first condition (where the multi-domain state is formed before the application of SAW), the magnetic field is applied along the transverse (i.e., y–) direction, and for the second condition, i.e., where the multi-domain state transitions to the single domain state after the application of SAW, the magnetic field is applied along the longitudinal (i.e., x–) direction.

A significant contrast is evident in the simulated hysteresis loops before and after the application of Surface Acoustic Wave (SAW) conditions. First, considering the conditions before applying SAW, the hysteresis loops of the 20 nm [Figure 8(a)], 90 nm [Figure 8(b)], and 160 nm [Figure 8(c)] configurations exhibit a negligible coercive field (S-type), indicating that the y-axis serves as the easy axis for these nanowires. However, when the nanowires are patterned into nanodots, the hysteresis loop becomes rectangular [Figure 8(d)], with a comparatively larger coercive field of approximately 230 Oe. In this case, an almost rectangular hysteresis loop is observed, marked by a sharp drop in magnetization at an external field of –230 Oe. The observed drastic variation in hysteresis loops could be attributed to demagnetizing energy or dipolar magnetic coupling. Interestingly, the hysteresis loops confirm that the overall value alone does not contribute significantly to the phenomenon; instead, its spatial distribution plays a crucial role in complex spin wave distribution. Given our studied film thickness of 40 nm, it is reasonable to assume that a coherent magnetization rotation reversal mode mechanism takes place, leading to the observed hysteresis loop for patterned nanodot arrays.

After the application of SAW conditions, the hysteresis loops for 20 nm, 90 nm, and 160 nm configurations are drastically different from that of the nanodot array. The 20 nm and 90 nm configurations exhibit a step in the hysteresis loop, while the 160 nm configuration shows a quasi-rectangular hysteresis loop. All of them display a comparatively larger coercive field. Nevertheless, the nanodot array now changes to an almost zero coercivity hysteresis loop with negligible remanence, as shown in Figure 8(h). Notably, all nanowire dimensions (length = 512 nm, width = 120 nm, and thickness = 40 nm) are greater than the exchange length (3.82 nm, as calculated earlier) of FeGa. Therefore, deviations from uniform magnetization are expected. Since the thickness-to-width ratio ($40/120 = 0.33$) is ≤ 0.5, no reversal mode would be present in our system [36, 37]. The origin of such a hysteresis loop for square nanodots can be elucidated from the perspective of domain formation, as explained below.

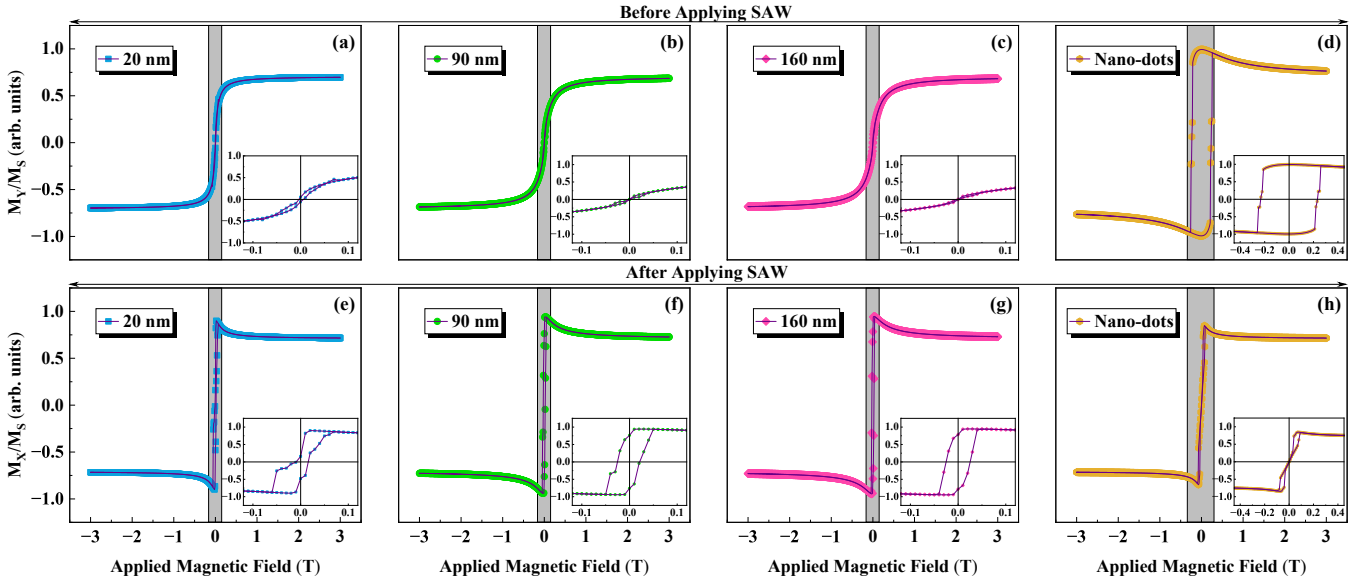


FIG. 8. Simulated hysteresis loops of 20 nm, 90 nm, 160 nm separated NWs (a)-(c) and the nanodots (d) before applying the SAW along transverse (y–) direction, while the same for the same configurations, (e)-(h) after the application of the SAW along longitudinal (x–) direction.

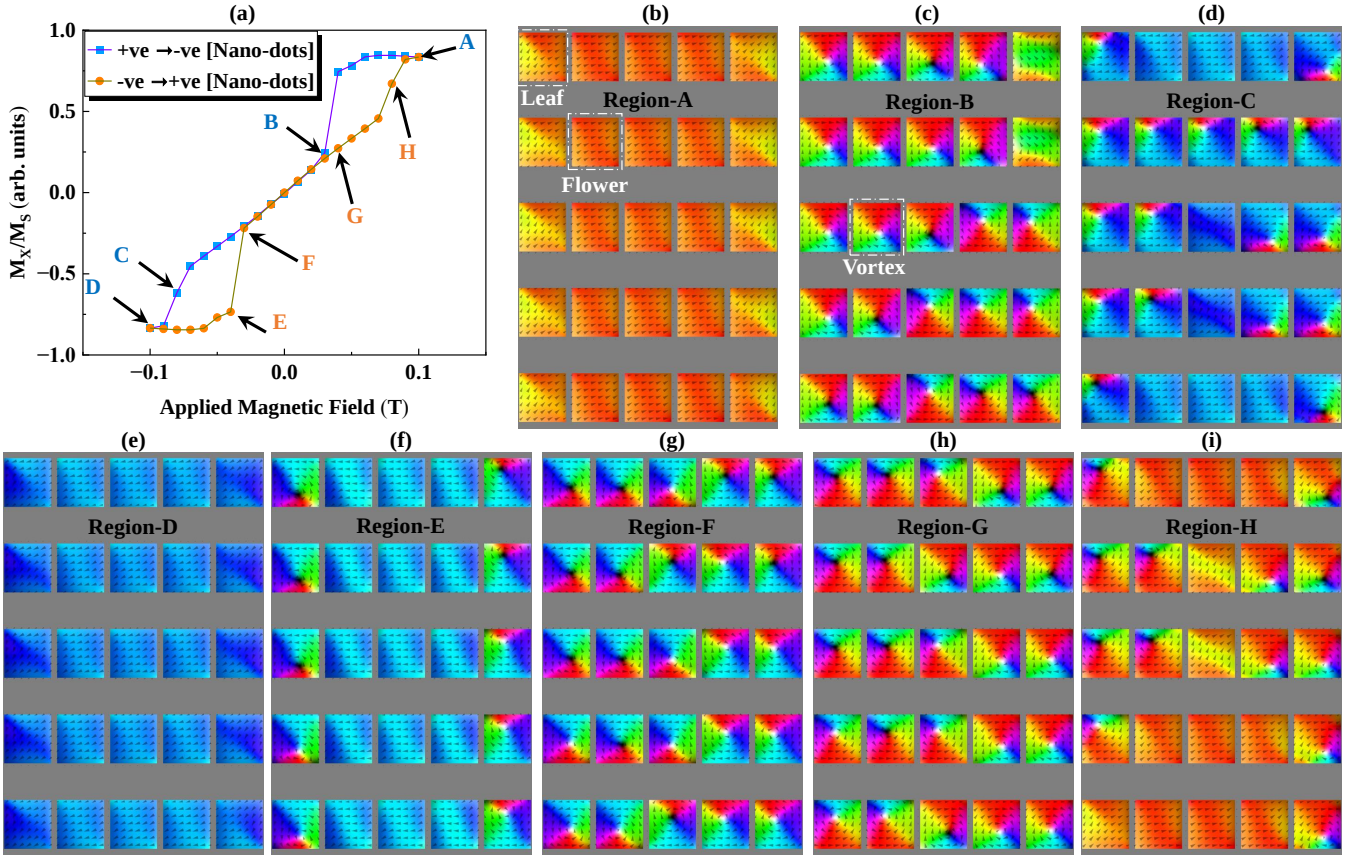


FIG. 9. Magnified (for field range ±0.1 T) simulated hysteresis loop for the square nanodot matrices after applying the SAW along longitudinal (x–) direction, where 'A'-'H' signifying the different position of magnetic field which are shown in (b)-(i), respectively. *'Flower'* (parallel to the longitudinal axis), *'Leaf'* (domains parallel to the diagonal of the nanodots), *'Vortex'* (flux closure of the magnetization) are highlighted to signify different domain states originated in the square nanodot matrix.

Figure 9(a) displays the magnified hysteresis loop (±0.1 T, magnetization saturation already occurs at this field) for the square nanodots matrix, while Figs. 9(b)-(h) illustrate various magnetic domain configurations corresponding to different magnetic field values along the hysteresis loop. The blue curve with square dots represents the field variation from +0.1 T to –0.1 T, while the orange curve with circular dots depicts the field reversal from –0.1 T to +0.1 T. Previous studies have indicated that exchange and demagnetization energy play a more crucial role than anisotropy energy in stabilizing domains [38]. In this context, the domain configurations primarily consist of different orientations, namely the *'Flower'*, *'Leaf'*, and *'Vortex'* states [38], highlighted in Figure 9(b)

Figure 9(b) illustrates a mixture of domain states at the +0.1 T applied magnetic field (position 'A' in Figure 9(a)), where both *leaf* and *flower* states coexist. As the field is reduced to +0.03 T after remanence, the *leaf* and *flower* states begin to transition toward *vortex* states [position 'B'; Figure 9(c)]. The E_{15} and E_{25} elements indicate the formation of 'S'-type domains, which can be considered a pre-*vortex* state at that field. When the magnetic field is further reduced to –0.08 T, the domain configuration of position 'C' in Figure 9(d) shows that the *leaf* states change their orientation, attempting to align themselves with the direction of the applied magnetic field. However, this field is insufficient to orient the *vortex* states into either *leaf* or *flower* states. All domains fully convert to a mixed *leaf* and *flower* state, where the states (position 'D') align in the reversed field direction, as depicted in Figure 9(e), towards the opposite direction of the domains in Figure 9(b). Now, if we consider the opposite direction, i.e., when the field is reversed from –0.1 T to +0.1 T. As the field increases to –0.04 T, the domain configuration (position 'E') in Figure 9(f) shows a coexistence of *vortex* and *flower* states. *vortex* states are generated on the edge elements, while *leaf* states lie in the middle elements. Upon further increasing and 9(c). When the domains are parallel to the longitudinal axis, they are referred to as the *'flower'* state, while those parallel to the diagonal are known as the *'leaf'* state. For *'vortex'* states, the domains are arranged in magnetization flux closure states. Typically, a significant difference between magnetostatic energy and exchange energy is observed for a *flower* state and a *leaf* state [38], with magnetostatic energy considered dominant over the exchange energy. However, a less variation in exchange and magnetostatic energy is observed for a *vortex* state. Subsequent sections elucidate the different domain states formed at varying applied magnetic fields.

the field to –0.03 T, the domain configuration (position 'F') in Figure 9(g) reveals that *vortex* states are generated within each of the elements. As the field is further increased to +0.04 T, the domain configuration (position 'G') in Figure 9(h) shows that *vortex* states remain in the *vortex* state. However, a closer look reveals that they now try to orient towards the positive side of the applied magnetic field. This subtle variation can be identified by the element color distribution; *vortex* states in position 'F' were inclined towards the negative direction (identified by its mostly bluish nature), whereas *vortex* states in 'G' are aligned towards the positive direction (identified by its strong reddish nature).

Before saturation, the domain state of position 'H' in Figure 9(i) shows that *leaf* states are now coexisting with the *vortex* states. When the matrix is fully saturated with a +0.1 T magnetic field, the domain configurations again become similar to that of Figure 9(b). On the contrary, for continuous nanowires are mostly formed with *flower* state (not shown here) thus signifying the dominance of magnetostatic energy contribution over the exchange energy. Since these complex mixtures of domain states (*flower*, *leaf*, *vortex*) are formed in the square nanodots array, it is crucial to note that the energies are distributed throughout the elements in a similarly complex fashion. Since external applied bias magnetic fields can switch between different states it introduces tuneability in domain states at the cost of external bias magnetic fields. Now, the following section elucidates the opportunity to utilize these MMA in the prospect of reservoir computing [15, 16].

III. PROSPECTS OF RESERVOIR COMPUTING WITH MMA

Initially, we explored the nonvolatile behavior of magnetic domains under bias-field free conditions in section II C. This investigation laid the foundation for understanding how domain configurations, in the absence of an external magnetic field, retain their magnetization states. These nonvolatile states are crucial for information processing in reservoir computing, where the system's internal dynamics must maintain and manipulate input signals over time.

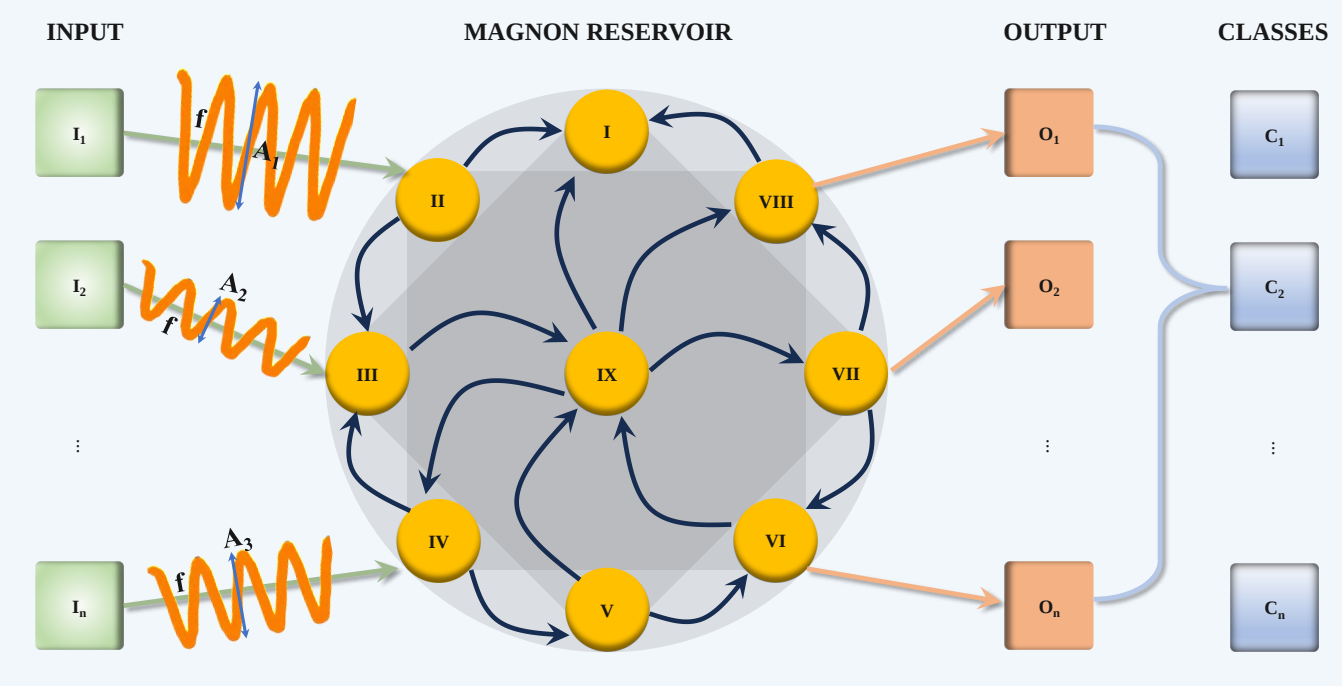


FIG. 10. Illustration of reservoir computing to handle the amplitude variation (from A_1 to A_n) at the constant input frequency (f). I_{1-n} are the inputs to the magnon reservoir with the different sets of nanowires/nanodots array configurations (e.g., I to IX are such nine arrays). The reservoir yield the results into different outputs, O_{1-9} and subsequently, categorised into different classes, C_{1-n} depending upon the results.

Subsequently, we examined the nonlinear behavior of the MMA system across different configurations, except for the 90 nm separation case. In configurations other than 90 nm, the output frequencies deviated from the input frequency, demonstrating the nonlinear frequency responsea key feature for reservoir computing. Conversely, the 90 nm configuration exhibited linear behavior, where the output frequency synchronized with the input, demonstrating phase locking. This behavior aligns with the principles of linear reservoirs, where the system responds in a predictable manner. The rich power-phase profiles revealed the intricate behavior of spin waves, showing complex dynamics in the phase space with variations in n_x and n_y. These profiles play a crucial role in mapping input signals into a high-dimensional phase space, which is a fundamental aspect of reservoir computing.

In contrast, the preceding section II E uncovered the ability to tune domain configurations within nanowires/nanodots using an external bias magnetic field. When an external

magnetic field is applied, the SAW excitation can preserve the altered domain configuration, further enriching the power-phase behavior due to changes induced by the magnetic field. This leads to a frequency shift governed by the Kittel formula, $f_\kappa = \sqrt{H_{ext} \cdot (H_{ext} + 4\pi M_{Sat})}$. This frequency shift establishes a direct link to reservoir computing by providing a mechanism to generate distinct frequencies (e.g., f_1 and f_2) as a function of the external magnetic field (H_{ext}). The ability to generate multiple distinct frequencies is essential for mapping input signals into different states in a high-dimensional phase space, which is at the heart of reservoir computing. By controlling the external magnetic field, the MMA can create a range of output frequencies, each representing a different state in the reservoir.

This capacity to modulate frequencies at varying H_{ext} values enables the MMA to serve as an adaptive reservoir, where input signals are processed and mapped to distinct outputs. This behavior aligns with the concept of signal mapping in reservoir computing, where the system transforms inputs into a wide variety of internal states that are later used to solve computational tasks like pattern recognition, classification, and time-series prediction [13].

A. Bias-Field Free Approach for Reservoir Computing

While the ability to tune domains and frequencies in the presence of external magnetic fields is valuable, our primary focus is on bias-field-free operation. In this configuration, the MMA operates without any external magnetic field, relying solely on the internal magnetization dynamics driven by phonon-magnon coupling and the intrinsic properties of the nanowires/nanodots. This approach offers significant advantages for energy-efficient computing and practical applications where bias-field-free operation is desirable.

We propose a novel approach to reservoir computing that focuses on amplitude variation rather than frequency variation. The traditional frequency-based method, such as the vowel recognition study conducted using spin torque nano-oscillators (STNOs) [39], demonstrated the power of reservoir computing by using frequency variations to process inputs. However, in practical speech recognition or other real-world tasks, both frequency and amplitude vary. Our approach aims to address this by using amplitude variations at a fixed operating frequency.

The schematic in Figure 10 illustrates how our MMA-based reservoir computing system can handle amplitude variations. In this setup:

(i) The inputs I_1, I_2, …, I_n correspond to different input signals fed into the magnon reservoir, which consists of various nanowire/nanodot configurations.

(ii) Each configuration operates at the same frequency (f) but with varying amplitude levels (A_1, A_2, …, A_n).

(iii) The reservoir processes these inputs, generating corresponding outputs O_1, O_2, …, O_n, which are categorized into distinct classes C_1, C_2, …, C_n based on the results.

By varying the amplitude at a fixed frequency, the system can effectively handle real-world signals where amplitude fluctuations are common. This approach offers further advancements in understanding the potential of reservoir computing and broadens the scope of applications beyond frequency-dependent tasks. In particular, this amplitude-based reservoir approach could be beneficial for applications like speech recognition, time-series analysis, and classification tasks where amplitude variation plays a key role. Here, we have introduced the potential of using the MMA as a reservoir computing system by leveraging its unique spin-wave dynamics, nonlinear behavior, and tunability under bias-field-free conditions. A comprehensive study of MMA-based reservoir computing will be presented in future work, where we will explore detailed applications and performance metrics of this approach in various computational tasks.

B. Stress Induced Frequency Tuning

In the previous section, we demonstrated that an additional external sine pulse fails to disrupt synchronization and frequency tunability. However, by keeping the input frequency constant and varying the stress value, we observed that the frequency-locked state disappears, allowing for tunability and introducing non-linearity into the system. Notably, since MuMax^3 does not directly incorporate stress, we modeled stress as a function of the anisotropy value. The stress-induced variations in magnetization oscillation and the corresponding frequency distribution are shown in Figure 11(a) and (b), respectively. Values of $K = 100, 300, 600, 800, 900, 1000$ reveal proper synchronized sinusoidal oscillation, while values of $K = 200, 400, 500, 700$ exhibit disrupted synchronization and introduce inherent non-linearity into the system. We further explored the synchronization behavior by performing the FFT of the magnetization oscillation. The frequency spectra revealed five distinct regions: *I* (from 0 to 0.75 GHz),

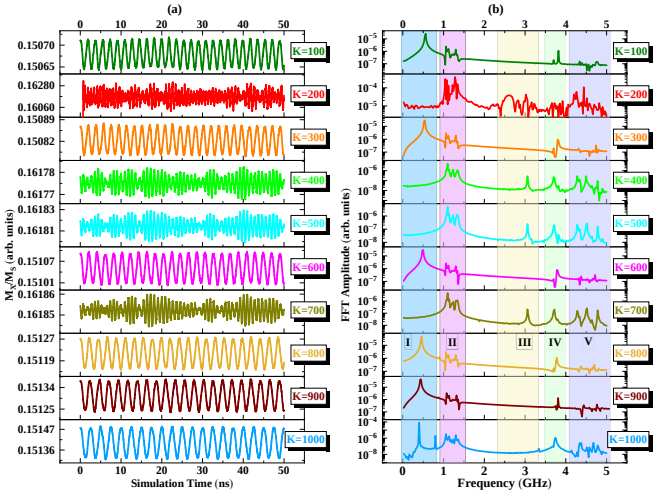


FIG. 11. Variation of (a) magnetization oscillation and (b) its corresponding frequency as a function of applied stress.

II (from 0.8 to 1.5 GHz), *III* (from 2.3 to 3.5 GHz), *IV* (from 3.5 to 4.0 GHz), and *V* (from 4.2 to 5.0 GHz), as highlighted in Figure 11(b). Most operating frequencies lie in region *I*, where the highest FFT amplitude is observed. A closer insight to the region *I* reveals that the frequency decreases with increasing stress. Region *IV* exhibits similar frequency tunability. However, regions *II* and *V* show contrasting behavior, indicating synchronization in the system. Notably, for $\mathrm{K} = 200, 400, 500, 700$, the operating frequency shifts to region *II*. Region *III* displays irregularity; for instance, $\mathrm{K} = 200$ shows higher amplitude and different behavior compared to the others. Therefore, this stress variation offers simultaneous frequency synchronization and tunability, which is advantageous for reservoir computing.

Tunability of hyperparameters in the software-based machine learning is capable of performing different computational tasks. However, the 'physical' reservoir computing schemes lack such critical functionality, which utilizes nonlinear and history-dependent responses of physical systems for data processing. Here, we propose to utilize the complex nonlinearites present in the modulated spin waves, generated out of the synchronization and desynchronization behaviour within the different nanowires/nanodots matrices. The required functional tunability could potentially be addressed with amplitude dependent training of different combination of NWs/NDs parameters, such as NWs/NDs dimensions, topologies, material parameters and array matrices. Additionally, the combination of complex nonlinear magnon power-phase distributions can potentially be leveraged in reconfguration of the key reservoir properties, such as nonlinearity, memory capacity, and complexity that would be capable of optimizing the computational performance across a diverse task set.

IV. CONCLUSION

In conclusion, our investigation focused on the power and phase profiles of spin waves within magnetostrictive nanowires (NWs) forming a nano-patterned "Magnon Microwave Antenna" (MMA) on a piezoelectric substrate under bias field free conditions. In order to stimulate the magnetization precession within the NWs, surface acoustic waves (SAW) onto the piezoelectric substrate were launched. It is demonstrated that magnetostriction, exchange, and dipolar interactions all contribute to the overall behavior of the system, but the dominant interactions can vary based on the specific configuration of the nanostructures (nanowires vs. nanodots) and the separation between them. The power-phase analysis revealed complex quantization numbers for various NW configurations, indicating intricate synchronization processes within the nanowires/nanodots. The ability to control and manipulate spin waves at both power and phase levels is pivotal for practical applications. Notably, the MMA, operating without an external bias magnetic field, lacks the fundamental Kittel mode, enabling the establishment of a frequency-locking state up to 500 GHz. This frequency-locked MMA demonstrated high stability in the time domain over an 80 ns simulation time span. Static magnetic studies unveiled square hysteresis loops or stepped hysteresis loops under different conditions (pre and post SAW application). The subsequent domain analysis confirmed the generation of three distinct domain states – *flower*, *leaf*, and *vortex* states – in the square nanodot array. Moreover, it demonstrated that the non-volatile domains generated under bias field free conditions could be tuned by applying an external magnetic field, presenting an opportunity for cutting-edge magnonic applications. Furthermore, we introduced an alternative approach for on-chip reservoir computing operating at the same frequency with varying amplitude. This innovative structure not only underscores the flexibility for further miniaturization of existing device sizes but also represents a noteworthy contribution to the evolving landscape of spintronics applications and development of energy-efficient and multifunctional magnonic devices.

AUTHOR CONTRIBUTIONS

A.S. and S.R. conceived the idea. S.R. brought the necessary research grant. A.S. performed all the COMSOL and micromagnetic simulations (with MuMax^3). A.S. took a major role in analysing the data and writing the original draft of the manuscript in conjunction with S.R..

ACKNOWLEDGEMENTS

The authors thank Science Foundation Ireland (SFI) Frontiers for the Future Programme (FFP) Award Grant (Grant ID: SFI-21/FFP-A/10003-MERIT) and NSF-SFI-DFE within the US-Ireland program (the associated Irish project grant ID: SFI-22/US/3852-nano-antenna) for funding this work.

SUPPORTING INFORMATION

Supplementary Text; Figures S1 to S6; Table S1

[1] S. Blundell, *Magnetism in Condensed Matter* (Oxford University Press, 2001).

[2] A. Samanta, G. Gubbiotti, and S. Roy, Spin waves in exchange spring nanoheterostructured amorphous/nanocrystalline films, Phys. Rev. B **107**, 214449 (2023).

[3] Q. Mistral, J.-V. Kim, T. Devolder, P. Crozat, C. Chappert, J. A. Katine, M. J. Carey, and K. Ito, Current-driven microwave oscillations in current perpendicular-to-plane spin-valve nanopillars, Applied Physics Letters **88**, 192507 (2006).

[4] D. Kumar, K. Konishi, N. Kumar, S. Miwa, A. Fukushima, K. Yakushiji, S. Yuasa, H. Kubota, C. V. Tomy, A. Prabhakar,

Y. Suzuki, and A. Tulapurkar, Coherent microwave generation by spintronic feedback oscillator, Scientific Reports **6**, 30747 (2011).
[5] D. A. Allwood, G. Xiong, C. C. Faulkner, D. Atkinson, D. Petit, and R. P. Cowburn, Magnetic Domain-Wall Logic, Science **309**, 1688 (2005).
[6] J. Åkerman, Toward a Universal Memory, Science **308**, 508 (2005).
[7] S. S. P. Parkin, M. Hayashi, and L. Thomas, Magnetic Domain-Wall Racetrack Memory, Science **320**, 190 (2008).
[8] A. Samanta and S. Roy, Generation of Microwaves With Tuneable Frequencies in Ultracompact Magnon Microwave Antenna via Phonon-Magnon-Photon Coupling, IEEE Transactions on Electron Devices **70**, 335 (2023).
[9] R. Fabiha, J. Lundquist, S. Majumder, E. Topsakal, A. Barman, and S. Bandyopadhyay, Spin Wave Electromagnetic Nano-Antenna Enabled by Tripartite Phonon-Magnon-Photon Coupling, Advanced Science **9**, 2104644 (2022).
[10] A. De, J. L. Drobitch, S. Majumder, S. Barman, S. Bandyopadhyay, and A. Barman, Resonant amplification of intrinsic magnon modes and generation of new extrinsic modes in a two-dimensional array of interacting multiferroic nanomagnets by surface acoustic waves, Nanoscale **13**, 10016 (2021).
[11] F. Chicco, A. Pezzotta, and C. C. Enz, Analysis of power consumption in LC oscillators based on the inversion coefficient, in *2017 IEEE International Symposium on Circuits and Systems (ISCAS)* (2017) pp. 1–4.
[12] S. Bhatti and S. N. Piramanayagam, High Amplitude Microwave Generation Using Domain Wall Motion in a Nanowire, physica status solidi (RRL) Rapid Research Letters **13**, 1800479 (2019).
[13] D. D. Yaremkevich, A. V. Scherbakov, L. De Clerk, S. M. Kukhtaruk, A. Nadzeyka, R. Campion, A. W. Rushforth, S. Savelev, A. G. Balanov, and M. Bayer, On-chip phonon-magnon reservoir for neuromorphic computing, Nature Communications **14**, 10.1038/s41467-023-43891-y (2023).
[14] L. Körber, C. Heins, T. Hula, J.-V. Kim, S. Thlang, H. Schultheiss, J. Fassbender, and K. Schultheiss, Pattern recognition in reciprocal space with a magnon-scattering reservoir, Nature Communications **14**, 10.1038/s41467-023-39452-y (2023).
[15] Y. Zhong, J. Tang, X. Li, B. Gao, H. Qian, and H. Wu, Dynamic memristor-based reservoir computing for high-efficiency temporal signal processing, Nature Communications **12**, 10.1038/s41467-020-20692-1 (2021).
[16] M. Cucchi, C. Gruener, L. Petrauskas, P. Steiner, H. Tseng, A. Fischer, B. Penkovsky, C. Matthus, P. Birkholz, H. Kleemann, and K. Leo, Reservoir computing with biocompatible organic electrochemical networks for brain-inspired biosignal classification, Science Advances **7**, eabh0693 (2021), https://www.science.org/doi/pdf/10.1126/sciadv.abh0693.
[17] COMSOL AB, COMSOL Multiphysics® Version 6.0. (2022).
[18] A. Vansteenkiste, J. Leliaert, M. Dvornik, M. Helsen, F. Garcia-Sanchez, and B. Van Waeyenberge, The design and verification of MuMax^3, AIP Advances **4**, 107133 (2014).
[19] J. L. Drobitch, A. De, K. Dutta, P. K. Pal, A. Adhikari, A. Barman, and S. Bandyopadhyay, Extreme Subwavelength Magnetoelastic Electromagnetic Antenna Implemented with Multiferroic Nanomagnets, Advanced Materials Technologies **5**, 2000316 (2020).
[20] D. Bhattacharya, M. M. Al-Rashid, N. D'Souza, S. Bandyopadhyay, and J. Atulasimha, Incoherent magnetization dynamics in strain mediated switching of magnetostrictive nanomagnets, Nanotechnology **28**, 015202 (2016).
[21] M. S. Fashami, J. Atulasimha, and S. Bandyopadhyay, Magnetization dynamics, throughput and energy dissipation in a universal multiferroic nanomagnetic logic gate with fan-in and fan-out, Nanotechnology **23**, 105201 (2012).
[22] Z. Xiao, R. Lo Conte, C. Chen, C.-Y. Liang, A. Sepulveda, J. Bokor, G. P. Carman, and R. N. Candler, Bi-directional coupling in strain-mediated multiferroic heterostructures with magnetic domains and domain wall motion, Scientific Reports **8**, 5207 (2018).
[23] A. Samanta and S. Roy, Investigation of transverse exchange-springs in electrodeposited nano-heterostructured films through first-order reversal curve analysis, APL Materials **12**, 091118 (2024).
[24] A. Hubert and R. Schäfer, *Magnetic domains: the analysis of magnetic microstructures* (Springer Science & Business Media, 2008) Chap. 3 and 5.
[25] K. Schultheiss, R. Verba, F. Wehrmann, K. Wagner, L. Körber, T. Hula, T. Hache, A. Kákay, A. A. Awad, V. Tiberkevich, A. N. Slavin, J. Fassbender, and H. Schultheiss, Excitation of Whispering Gallery Magnons in a Magnetic Vortex, Phys. Rev. Lett. **122**, 097202 (2019).
[26] S. Dutta, A. Samanta, S. N. Panda, S. Roy, and A. Barman, Ultrafast demagnetization and Gilbert damping in electrodeposited CoP film, Journal of Materials Science **58**, 14817 (2023).
[27] J. M. Shaw, W. H. Rippard, S. E. Russek, T. Reith, and C. M. Falco, Origins of switching field distributions in perpendicular magnetic nanodot arrays, Journal of Applied Physics **101**, 023909 (2007).
[28] Berk, Cassidy and Jaris, Mike and Yang, Weigang and Dhuey, Scott and Cabrini, Stefano and Schmidt, Holger, Strongly coupled magnon-phonon dynamics in a single nanomagnet, Nature Communications **10**, 2652 (2019).
[29] W.-G. Yang and H. Schmidt, Acoustic control of magnetism toward energy-efficient applications, Applied Physics Reviews **8**, 021304 (2021).
[30] S. Mondal, M. A. Abeed, K. Dutta, A. De, S. Sahoo, A. Barman, and S. Bandyopadhyay, Hybrid Magnetodynamical Modes in a Single Magnetostrictive Nanomagnet on a Piezoelectric Substrate Arising from Magnetoelastic Modulation of Precessional Dynamics, ACS Applied Materials & Interfaces **10**, 43970 (2018).
[31] Y. Yahagi, B. Harteneck, S. Cabrini, and H. Schmidt, Controlling nanomagnet magnetization dynamics via magnetoelastic coupling, Phys. Rev. B **90**, 140405 (2014).
[32] S. Bhatti, C. Ma, X. Liu, and S. N. Piramanayagam, Stress-Induced Domain Wall Motion in FeCo-Based Magnetic Microwires for Realization of Energy Harvesting, Advanced Electronic Materials **5**, 1800467 (2019).
[33] V. Sampath, N. DSouza, D. Bhattacharya, G. M. Atkinson, S. Bandyopadhyay, and J. Atulasimha, Acoustic-Wave-Induced Magnetization Switching of Magnetostrictive Nanomagnets from Single-Domain to Nonvolatile Vortex States, Nano Letters **16**, 5681 (2016).
[34] R. P. Cowburn, A. O. Adeyeye, and M. E. Welland, Configurational Anisotropy in Nanomagnets, Phys. Rev. Lett. **81**, 5414 (1998).
[35] S. Goolaup, A. O. Adeyeye, N. Singh, and G. Gubbiotti, Magnetization switching in alternating width nanowire arrays, Phys. Rev. B **75**, 144430 (2007).
[36] G. C. Han, B. Y. Zong, P. Luo, and Y. H. Wu, Angular dependence of the coercivity and remanence of ferromagnetic nanowire arrays, Journal of Applied Physics **93**, 9202 (2003).

[37] S. Goolaup, N. Singh, A. O. Adeyeye, V. Ng, and M. B. Jalil, Transition from coherent rotation to curling mode reversal process in ferromagnetic nanowires, The European Physical Journal B - Condensed Matter and Complex Systems **44**, 10.1140/epjb/e2005-00122-7 (2005).

[38] M. Maicas, M. Rodrguez, E. López, M. Sánchez, C. Aroca, and P. Sánchez, Magnetic switching fields in square monolayer and bilayer nanodots, Computational Materials Science **25**, 525 (2002).

[39] M. Romera, P. Talatchian, S. Tsunegi, F. Abreu Araujo, V. Cros, P. Bortolotti, J. Trastoy, K. Yakushiji, A. Fukushima, H. Kubota, S. Yuasa, M. Ernoult, D. Vodenicarevic, T. Hirtzlin, N. Locatelli, D. Querlioz, and J. Grollier, Vowel recognition with four coupled spin-torque nano-oscillators, Nature **563**, 10.1038/s41586-018-0632-y (2018).